PNAS RESEARCH ARTICLE | CELL BIOLOGY OPEN ACCESS

Cryosectioning-enhanced super-resolution microscopy for single-protein imaging across cells and tissues

Johannes Stein[a,b,1], Maria Ericsson[c], Michel Nofal[a], Lorenzo Magni[a], Sarah Aufmkolk[b], Ryan B. McMillan[a], Laura Breimann[b], Conor P. Herlihy[b], S. Dean Lee[b], Andréa Willemin[d,e], Jens Wohlmann[f], Laura Arguedas-Jimenez[d], Peng Yin[a], Ana Pombo[d,e], George M. Church[a,b,1], and Chao-ting Wu[b,1]

Affiliations are included on p. 9.

Edited by Taekjip Ha, Children's Hospital Boston, Boston, MA; received February 27, 2025; accepted July 2, 2025

DNA-points accumulation for imaging in nanoscale topography (DNA-PAINT) enables nanoscale imaging with virtually unlimited multiplexing and molecular counting. Here, we address challenges, such as variable imaging performance and target accessibility, that can limit its broader applicability. Specifically, we enhance its capacity for robust single-protein imaging and molecular counting by optimizing the integration of total internal reflection fluorescence microscopy with physical sectioning, in particular, Tokuyasu cryosectioning. Our method, tomographic and kinetically enhanced DNA-PAINT (tkPAINT), achieves 3 nm localization precision across diverse samples, enhanced imager binding, and improved cellular integrity. tkPAINT can facilitate molecular counting with DNA-PAINT inside the nucleus, as demonstrated through its quantification of the in situ abundance of RNA Polymerase II in both HeLa cells as well as mouse tissues. Anticipating that tkPAINT could become a versatile tool for the exploration of biomolecular organization and interactions across cells and tissues, we also demonstrate its capacity to support multiplexing, multimodal targeting of proteins and nucleic acids, and three-dimensional (3D) imaging.

super-resolution microscopy | DNA-PAINT | single-molecule localization microscopy | nuclear organization | TIRF

Significance

Visualizing the spatial organization of biomolecules can advance our understanding of cellular function, yet achieving nanoscale resolution across diverse targets and samples remains challenging. This paper presents tomographic and kinetically enhanced DNA-points accumulation for imaging in nanoscale topography (tkPAINT), a fluorescence microscopy approach suited for single-protein imaging and relative molecular counting of specifically labeled targets—for example, through immunolabeling—in cells and tissues. By optimizing the integration of physical sectioning with DNA-points accumulation for imaging in nanoscale topography (DNA-PAINT) super-resolution microscopy, tkPAINT maximizes imaging precision, structural integrity, and molecular accessibility. This approach enables detailed studies of biomolecular organization and interactions and expands the capabilities of fluorescence microscopy in cell biology and biomedical research.

Spatial omics technologies are advancing our understanding of the molecular principles that govern cellular function and organization (1–3). By integrating molecular composition with spatial context, these approaches illuminate how biomolecules organize within cells and tissues. Super-resolution microscopy has expanded these capabilities, enabling visualization of biomolecules at sub-20 nm resolution (4–7). DNA-points accumulation for imaging in nanoscale topography (DNA-PAINT) is a single-molecule localization microscopy (SMLM) technique that achieves super-resolution imaging via transient binding of dye-labeled "imager" oligonucleotides to complementary "docking strands" attached to the target molecules (8). DNA-PAINT enables straightforward sequential multiplexing of up to 30 targets (9–11), single-protein resolution (12–14), and molecular counting (15, 16), establishing it as a powerful tool for spatial biology.

The potential of DNA-PAINT relies on sample preparations that ensure accessibility to a wide range of targets while retaining cellular ultrastructure. Indeed, challenges such as fixation-induced redistribution of target molecules, antibody-induced clustering, or target loss during permeabilization can affect nanoscale imaging outcomes (17–21). Additionally, the imaging performance of DNA-PAINT varies across sample types, molecular targets, and microscopy modalities (8, 22, 23). For instance, while Total Internal Reflection Fluorescence (24) (TIRF) microscopy offers the highest resolution for single-protein imaging with DNA-PAINT (12, 14), its axial range (~200 nm) restricts imaging to targets near the cover glass. Most cellular targets, however, elude the accessible TIRF range and thus require alternative imaging conditions, reducing resolution (8, 22, 23) and limiting its ability for counting (12, 13, 25–28).

Physical sectioning offers compelling solutions to these challenges (29–32), enabling TIRF-based SMLM imaging of cell regions otherwise inaccessible (33) while ensuring high target accessibility and structural integrity (34, 35). Despite implementations with SMLM across diverse samples (33, 36–40), sectioning has thus far only been used for DNA-PAINT imaging of tissues (41–45), where it is a routine step. For instance, Tokuyasu cryosectioning (46)—known for its superior ultrastructure preservation and antigenicity compared to resin sectioning (35)—was recently adopted for DNA-PAINT (47, 48), achieving 4 nm localization precisions using TIRF and multiplexing via Exchange-PAINT (9) on ~350 nm rat brain cryosections without permeabilization. Additionally, DNA-PAINT imaging of ultrathin resin sections has enabled volumetric reconstructions from sequential sections, as shown in

Preprint server: A preprint of this manuscript was uploaded to bioRxiv.com under a C-BY-NC-ND 4.0 license (https://doi.org/10.1101/2024.02.05.576943).

This article is a PNAS Direct Submission.

[1]To whom correspondence may be addressed. Email: johannes.stein@wyss.harvard.edu, gchurch@genetics.med.harvard.edu, or twu@genetics.med.harvard.edu.

This article contains supporting information online at https://www.pnas.org/lookup/suppl/doi:10.1073/pnas.2504578122/-/DCSupplemental.

Published August 7, 2025.

Alzheimer's brain tissues (45). These studies provide compelling reasons to maximize the potential of physical sectioning for DNA-PAINT. Key questions remain regarding how physical sectioning can generally improve performance and applicability of DNA-PAINT, particularly in nontissue samples such as cultured cells that do not inherently require sectioning prior to imaging. Additionally, physical sectioning could be used as a tool to enhance imager binding statistics, enabling to count molecules where this is otherwise challenging to achieve.

Here, we present "tomographic and kinetically enhanced DNA-PAINT" (tkPAINT), a workflow that leverages physical sectioning to align sample volume with TIRF illumination, thereby greatly enhancing resolution and imager binding for robust single-protein imaging and counting. Adopting a Tokuyasu protocol for targeting RNA Polymerase II (Pol II) in HeLa cells (49), we demonstrate the potential of physical sectioning for intranuclear DNA-PAINT imaging (22, 50–54) (Fig. 1*A*), obtaining localization precisions down to 3 nm while preserving cellular ultrastructure. We show that reducing section thickness can enhance imager binding statistics, with up to 80% of localizations attributed to Pol II signal in ~150 nm cryosections. This enabled us to perform relative molecular counting of immunolabeled targets with DNA-PAINT inside the nucleus. Using qPAINT (15) (quantitative DNA-PAINT), we count antibodies within nanoscopic Pol II clusters and quantify their nuclear abundance. Extending tkPAINT to mouse tissues, we demonstrate its ability to deliver consistent conditions for single-protein imaging and counting across sample types while revealing cell- and tissue-specific heterogeneities in Pol II organization (55, 56). The versatility of tkPAINT is further highlighted through multiplexing, multimodal imaging of proteins and nucleic acids as well as 3D imaging using astigmatism. While this work pushes the capabilities of DNA-PAINT for spatial biology in single sections, we anticipate integrations of tkPAINT with well-established serial sectioning approaches (36, 39, 45, 57) to reconstruct larger sample volumes and entire nuclei.

Results

TIRF-Based DNA-PAINT throughout Ultrastructure-Preserved Cells Enhances Resolution and Binding Kinetics. To develop tkPAINT, we chose to target the largest subunit of Pol II, Rpb1,

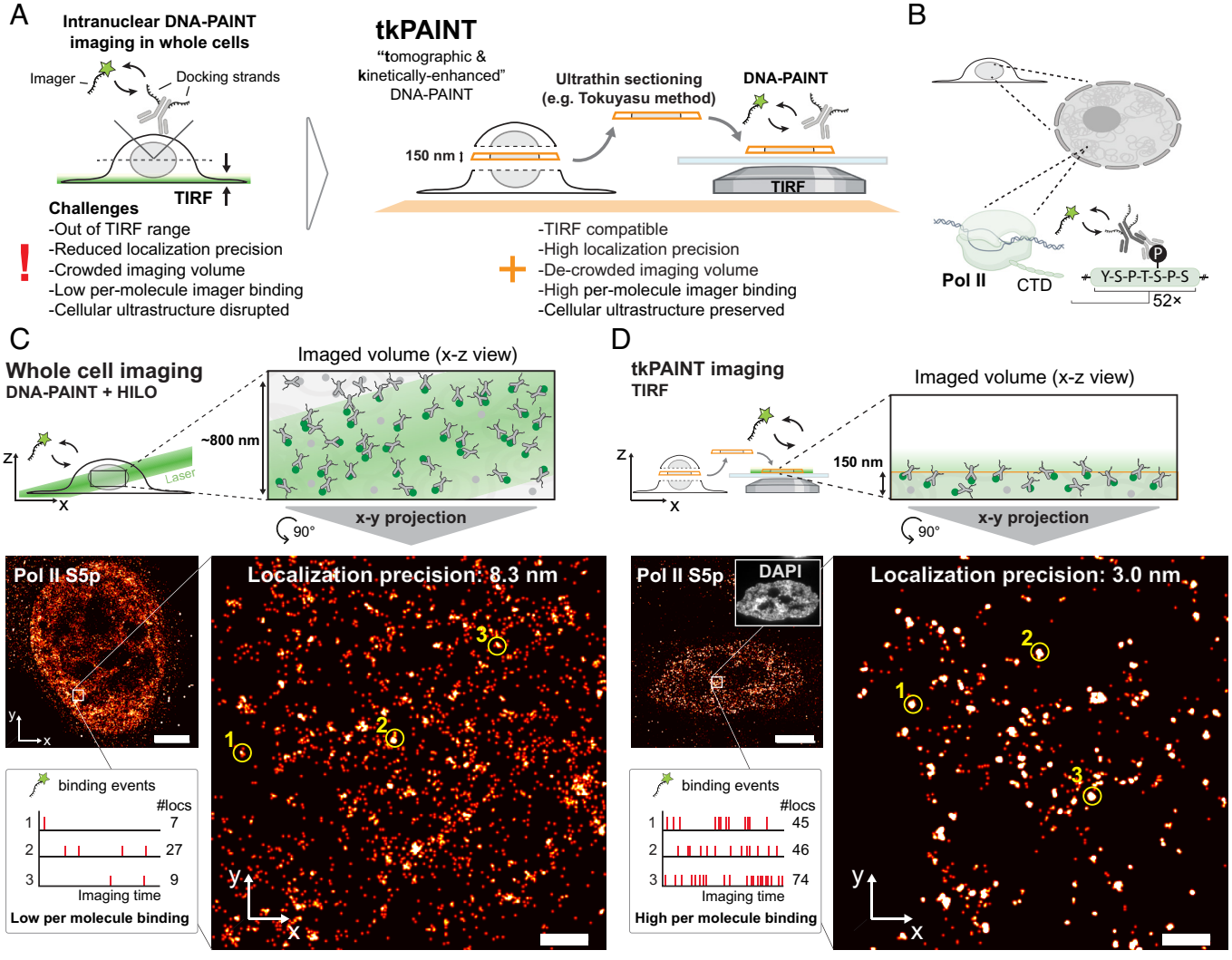

Fig. 1. tkPAINT enables TIRF-based DNA-PAINT imaging of intranuclear targets and enhanced imager binding. (*A*) tkPAINT schematic. Ultrathin cryosectioning enables nuclear DNA-PAINT imaging under TIRF conditions. (*B*) Immunolabeling of Pol II CTD Serine-5 phosphorylation (S5p) for DNA-PAINT imaging via docking strand-conjugated secondary antibodies. (*C*) HILO DNA-PAINT image of Pol II S5p within whole HeLa cell. Time traces of imager binding and corresponding number of localizations are shown for the three regions indicated by yellow circles, demonstrating low per-molecule binding since imager binding events are shared between a high number of labeled target molecules within the imaged volume (green circles, top schematic; gray target molecules inaccessible to antibody labeling remain unseen). (*D*) tkPAINT image of Pol II S5p. The *Inset* shows the same cell imaged in the DAPI channel. Time traces of imager binding and number of localizations are shown for three regions indicated by yellow circles, demonstrating high per-molecule binding. Imager binding events are shared between a low number of imaged target molecules within the imaged volume (green circles, top schematic). Scale bars, 5 μm in (*C* and *D*), 400 nm in zoom-ins.

a highly abundant nuclear protein. We focused, in particular, on its C-terminal domain (CTD), which features 52 heptad repeats of the consensus motif YSPTSPS, the residues of which are posttranslationally modified during transcription and are involved in promoting cotranscriptional RNA splicing (58) (Fig. 1*B*). Using a primary antibody against hyperphosphorylated Serine-5 of the CTD (S5p), we then leveraged previously optimized protocols for diffraction-limited nuclear imaging within Tokuyasu cryosections under ultrastructure-preserving conditions (59) (*SI Appendix*, Fig. S1). If not stated otherwise, we refer to ultrathin cryosections of ~150 nm thickness as "cryosections," which were used for most tkPAINT experiments presented in this work.

We labeled whole HeLa cells as well as cryosections of fixed HeLa cells with both primary antibodies and oligo-conjugated secondary antibodies designed for two-dimensional (2D) DNA-PAINT imaging using both a classical imager (8) (P1) and speed-optimized imager (60) (R4) which enables faster imaging at reduced imager concentrations and hence reduced fluorescence background (*Materials and Methods*). Whole cells were then imaged using DNA-PAINT with HILO illumination, while for tkPAINT, cryosections were imaged using TIRF illumination with the incidence angle set just above the critical angle, allowing sufficient illumination throughout the section depth of 150 nm, preventing loss of single-molecule signals. For HILO imaging we increased imager concentrations by twofold to fourfold compared to tkPAINT, due to bleaching of diffusing imagers within the excited HILO volume, reducing the effective imager concentration. At least three datasets were acquired per condition. Duration of data acquisition was kept identical for both HILO DNA-PAINT and tkPAINT imaging, and imager concentrations were adjusted individually in each experiment to ensure sparse single-molecule blinking required for obtaining localizations from individual fluorescent molecules (6) (*Materials and Methods*).

Fig. 1 *C* and *D* depict the reconstructed super-resolution images obtained via HILO DNA-PAINT and tkPAINT, respectively. Overall, localizations appeared less clustered and more widely distributed in the HILO DNA-PAINT image presumably due to the larger imaging volume crowded with antibodies and to lower resolution. TIRF illumination in tkPAINT led to up to 10× higher signal-to-noise ratio, as compared to HILO (*SI Appendix*, Fig. S2), translating to an almost threefold improvement in localization precision, down to ~3 nm as compared to ~8.3 nm in HILO DNA-PAINT [determined via Nearest Neighbor Analysis (61), NeNA; *SI Appendix*, Fig. S2]. R4 enabled HILO imaging at 10× lower imager concentration compared to P1, increasing the signal-to-noise ratio by more than fourfold. However, this did not translate to an improvement in localization precision (8.1 nm vs. 8.3 nm, respectively; *SI Appendix*, Fig. S2), indicating that background fluorescence from diffusing imagers had negligible influence on localization precision. To confirm this, we used fluorogenic imager strands (11, 62) for HILO imaging, which suppress both fluorescence and photobleaching during diffusion, again achieving localization precisions of ~8 nm (*SI Appendix*, Fig. S3). The improved localization precision in tkPAINT thus likely arises from the smaller imaging volume itself, reducing sample autofluorescence and out-of-focus imager binding. Furthermore, single-molecule fluorescence events occur close to the cover glass, and thus, emitted photons travel a minimal distance through the cell's heterogeneous refractive index. In contrast, emitters located deeper within whole cells, as in HILO, are more prone to optical aberrations and scattering which can reduce the localization precision (22).

As a reference, we performed in vitro DNA-PAINT imaging of surface-immobilized DNA origami (63) structures that featured a docking strand pattern with 20 nm spacing (8) using TIRF. This resulted in a localization precision of 2.8 nm (*SI Appendix*, Fig. S4), demonstrating that tkPAINT can translate the resolution achievable with TIRF under in vitro conditions to the nuclei of fixed cells.

Efficient nuclear antibody staining in whole cells typically requires strong permeabilization (19), which can disrupt cellular ultrastructure, particularly in the cytoplasm (18) (*SI Appendix*, Fig. S5). This disruption limits the applicability of multiplexed DNA-PAINT imaging for detergent-sensitive cytoplasmic targets, such as lysosomes (64), alongside nuclear antigens. By enabling intracellular access through sectioning, omitting permeabilization, tkPAINT overcomes this limitation. We demonstrated simultaneous imaging of lysosome-associated membrane protein 1 (LAMP1) and RNA Polymerase II (Pol II) at sub-3 nm localization precision while preserving cellular ultrastructure, as validated by immunogold electron microscopy (*SI Appendix*, Fig. S5). In the nucleus, permeabilization did not lead to noticeable ultrastructural perturbation and can be used to enhance antigen accessibility throughout cryosections (65) (*SI Appendix*, Figs. S1 and S6).

In addition to enhancing resolution and enabling cell-wide ultrastructural access, ultrathin sectioning inherently improves the kinetic sampling of target molecules. The reduced imaged volume allows higher per-molecule imager-binding frequency while still ensuring isolated single-molecule fluorescence events required for accurate localization (*SI Appendix*, Fig. S7*A*). In fact, inspecting individual clouds of localizations in both datasets indicated significantly higher imager binding frequencies as well as number of localizations with tkPAINT as compared to HILO DNA-PAINT (yellow circles and *Insets*, Fig. 1 *C* and *D*, respectively). To confirm this, we globally analyzed both datasets by dividing them into five equal temporal segments and assigning unique colors to each segment (e.g., red for the first segment, blue for the last; total imaging time ~17 min; *SI Appendix*, Fig. S7*B*). The highly colored HILO image indicated most target molecules experienced only imager binding events during one of the time segments. In contrast, the tkPAINT image appeared predominantly white, reflecting frequent revisits of imagers to target molecules. The reduction in imaging volume with tkPAINT effectively enhances imager-binding statistics, a crucial factor in DNA-PAINT for both single-molecule profiling at high fidelity and molecular counting, as explained in the following section.

tkPAINT Enables Nuclear Imaging of Pol II at Single-Antibody Resolution and Molecular Counting. The repetitive binding of imagers in DNA-PAINT is a critical advantage for single-protein imaging, enabling the exclusion of localizations caused by nonrepetitive imager sticking (13, 66, 67). This is typically accomplished by employing clustering algorithms to identify accumulations of localizations, referred to as "localization clouds," which originate from docking strand-conjugated labels. The kinetic fingerprint of each localization cloud is then analyzed to determine whether it exhibits repetitive binding. Fig. 2*A* outlines this two-step analysis approach similar to the one by Fischer et al. (13), i) applying the clustering algorithm DBSCAN (68) to detect localization clouds and ii) using a kinetic filter to exclude clouds that lack repetitive binding and are likely attributable to nonspecific imager sticking (for a detailed description of DBSCAN clustering and kinetic filtering, see *SI Appendix*, Fig. S8).

For the tkPAINT datasets imaged with speed-optimized imager R4, over 80% of nuclear localizations were identified as repetitive localization clouds, demonstrating efficient and targeted imaging (Fig. 2*B*). In comparison, classic imager P1 yielded a postfiltering rate of 60%, consistent with the expected benefits of speed-optimized imagers (60, 69). Since multiple secondary antibodies can bind to

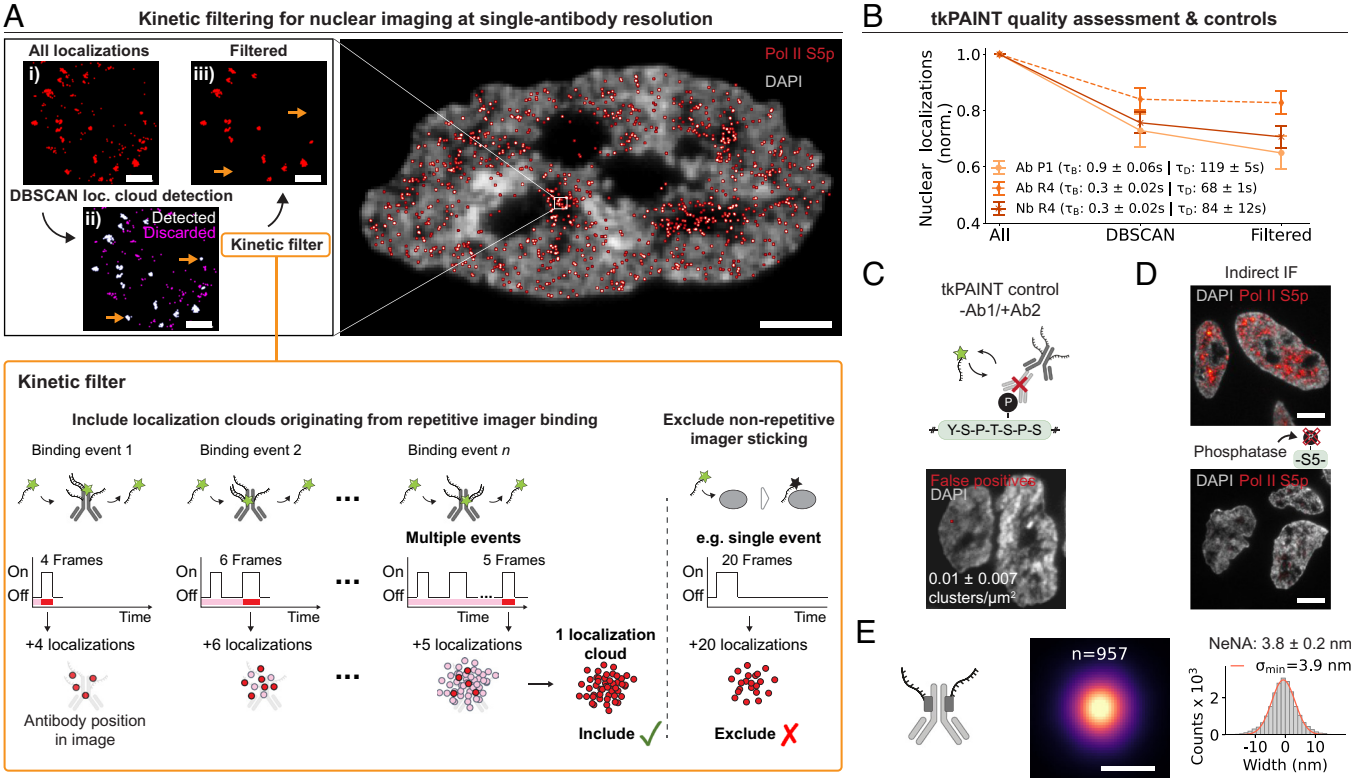

Fig. 2. Nuclear imaging of Pol II at single-antibody resolution via tkPAINT. (*A*) Schematic of tkPAINT data processing. i) Image showing all raw localizations. ii) DBSCAN clustering is applied to detect localization clouds (white), and remaining localizations are discarded (magenta). iii) A kinetic filter (66, 67) is applied to discard localization clouds originating from nonrepetitive imager sticking (orange arrows in ii) and iii); schematic description in orange box below and detailed in *SI Appendix*, Fig. S8). (*B*) Kinetic filter yield shown for tkPAINT Pol II S5p datasets imaged using different imager sequences [P1—classic (8) vs. R4—speed (60)] or different secondary labeling strategies: secondary antibody (Ab) vs. secondary nanobody (Nb). Normalized localization counts with respect to all initial nuclear localizations showing relative loss of localizations in each analysis step. The binding kinetics for each imager are given as mean bright and mean dark time (τ_B and τ_D, respectively. See *SI Appendix*, Fig. S8). n = 3 replicates, each with ≥10 cells. (*C*) tkPAINT negative control imaging of sample processed with the standard staining protocol but leaving out primary antibody and incubating secondary antibodies only. Mean and SD of number of false-positive localization clusters per nuclear area displayed. (*D*) *Top*: Diffraction-limited indirect immunofluorescence image of cryosections labeled for Pol II S5p (red) and DAPI (white). *Bottom*: same as *Left*, but cryosections were treated with phosphatase prior to immunostaining. (*E*) Localization precision benchmarking for Pol II S5p datasets based on secondary nanobody labeling. *Middle*: rendered sum images of center-of-mass aligned smallest identifiable localization clouds (see *SI Appendix*, Fig. S11 for details and additional datasets. Number of localization clouds in sum image stated above). *Right*: histogram showing the corresponding distribution of localizations fitted with a Gaussian (red curve) to obtain its SD σ_{min}. n = 3 replicates, each with ≥8,500 localization clouds from ≥10 cells. Error bars and errors in (*B* and *E*) correspond to mean and SD. Scale bars, 5 μm in (*A* and *E*), 3 μm in (*D*), and 10 nm in sum image in (*E*).

a single primary antibody, this may amplify imager binding at individual target epitopes. To assess this, we repeated tkPAINT imaging using R4-conjugated secondary nanobodies, which limit the number of docking strands to a maximum of two per primary antibody. We indeed observed a minor reduction compared to R4-labeled secondary antibodies, however, still providing an excellent postfiltering localization yield of ~70%.

However, repeated imager binding on its own is not necessarily indicative of specificity since intrinsic cellular features could potentially also lead to repeated binding. Furthermore, secondary labels could nonspecifically bind and thus position docking strands within the sample. To estimate the impact of false-positive localization clouds, we performed a set of negative controls under conditions identical to that of previous tkPAINT acquisitions, but on cryosections that were incubated only with secondary antibody/nanobody and no primary antibody (Fig. 2*C*). For all tkPAINT imaging conditions, we found a negligible contribution (~1%) of false-positive localization clouds in both cases as compared to tkPAINT experiments labeled with both primary and secondary antibody/nanobody (Fig. 2*C* and *SI Appendix*, Fig. S9). Increasing section thickness led to higher localization cloud densities but also mislocalizations due to simultaneously bound imagers, while, as expected, both localization precision and kinetic enhancement diminished (*SI Appendix*, Fig. S10). Thinner cryosections (~80 nm) as used in our immunogold electron microscopy experiments (*SI Appendix*, Fig. S5) yielded sparse antibody signal and required delicate handling, making 150 nm our default thickness for tkPAINT. Finally, we tested the specificity of the primary antibody against Pol II S5p by treating cryosections with phosphatase in order to neutralize phosphorylation sites prior to staining for indirect immunofluorescence (59). Reassuringly, this led to a threefold signal loss (Fig. 2*D*).

The sparse distribution of localization clouds after kinetic filtering in tkPAINT (Fig. 2*A*) was reminiscent of immunogold experiments in which antibodies labeled with gold nanoparticles (diameters ~5 to 15 nm) permit antigens to be detected in cryosections by TEM at the level of single antibodies (35). To determine whether the resolution possible through tkPAINT would enable single antibodies to be visualized, we performed a range of center-of-mass alignments to obtain averaged sum images for a decreasing minimum number of localizations per cloud (*SI Appendix*, Fig. S11). We found that localizations in sum images were approximately Gaussian distributed with their SD converging to a minimum. In other words, further reduction of localizations per cloud did not reduce the localization spread. Fig. 2*E* displays a convergent sum image with a SD (σ_{min}) of ~3.9 nm and a full width at half maximum of ~9 nm (FWHM ≈ 2.355×σ_{min}), indicating that localizations likely accumulated from individual antibodies, whose physical size is ~10 nm (70). Since secondary-nanobody labeling reduces the total label size, localization clouds more

accurately reflect underlying Pol II S5p epitope positions compared to the increased label size of secondary antibody labeling (*SI Appendix*, Fig. S11). Together with the controllable number of docking strands per primary antibody (up to two) we thus focused our efforts with tkPAINT to quantify nuclear Pol II S5p based on primary antibodies labeled with secondary nanobodies (R4).

Since several antibodies can likely bind to a single CTD or to several Pol II molecules close by, we asked whether we could exploit the enhanced imager binding kinetics in tkPAINT to count the number of Pol II antibodies in larger localization clouds (Fig. 3*A*). In qPAINT (15) (quantitative DNA-PAINT), the average imager binding frequency for the smallest identifiable localization clouds in a dataset is taken as a reference (Fig. 3*B*). Assuming the reference represents single antibodies, a localization cloud with N antibodies would have an N-times higher binding frequency, and thus the binding frequency of a localization cloud can be used for relative counting (15).

We first turned to DNA origami featuring up to 12 docking strands to validate the applicability of qPAINT analysis under our experimental tkPAINT conditions. Furthermore, on DNA origami single docking strands can be unambiguously chosen as reference clouds. Fig. 3*B* displays the counting results obtained via qPAINT analysis, confirming the expected number of on average ~8 docking strands per origami which was in good agreement with visual inspection (see *SI Appendix*, Fig. S12 for additional 400 randomly selected origami and analysis schematic), confirming our ability to perform molecular counting.

In tkPAINT Pol II S5p datasets, most sparse localization clouds likely corresponded to single antibodies according to the previously observed spatial localization spread. We thus performed qPAINT analysis using Pol II S5p localization clouds with a convex hull area smaller than the 20th percentile as the qPAINT reference (see *SI Appendix*, Fig. S13 for a detailed analysis schematic). Comparing the imager binding frequency of single docking strands on DNA origami with the one measured for single antibodies in tkPAINT datasets, we obtained on average ~1.6 bound nanobodies per primary antibody (*SI Appendix*, Fig. S13).

Fig. 3*C* displays the counting results (N) obtained from three independent experiments, each with a prominent single-antibody peak and a decreasing tail of localization clouds containing higher numbers of antibodies. The N distributions were in close agreement, with on average 3.2 ± 0.4 antibodies per localization cloud. Localization clouds containing tens of antibodies indicated hot spots of active Pol II (Fig. 3*C*). Based on these counting results and the known cryosection dimensions, we measured an average nuclear antibody density of 165 ± 45 μm^{-3}, which would translate to ~115,000 ± 42,000 Pol II S5p antibodies per nucleus using the average HeLa nuclear volume of 600 μm^3 as determined via confocal microscopy (Fig. 3*D*). Note that this quantification assumes that sampling a sufficient number of random nuclear sections provides an average estimate of total nuclear Pol II S5p, despite its highly heterogeneous spatial distribution. Future validations and orthogonal imaging in whole cells will be required to validate these results. It is further likely that our quantification underestimated the true abundance of phosphorylated S5 (in theory up to 52× per CTD) due to steric effects of antibody labeling. Smaller primary labels such as nanobodies against S5p could further improve quantifications and reduce linkage errors. Notably, we could not determine whether

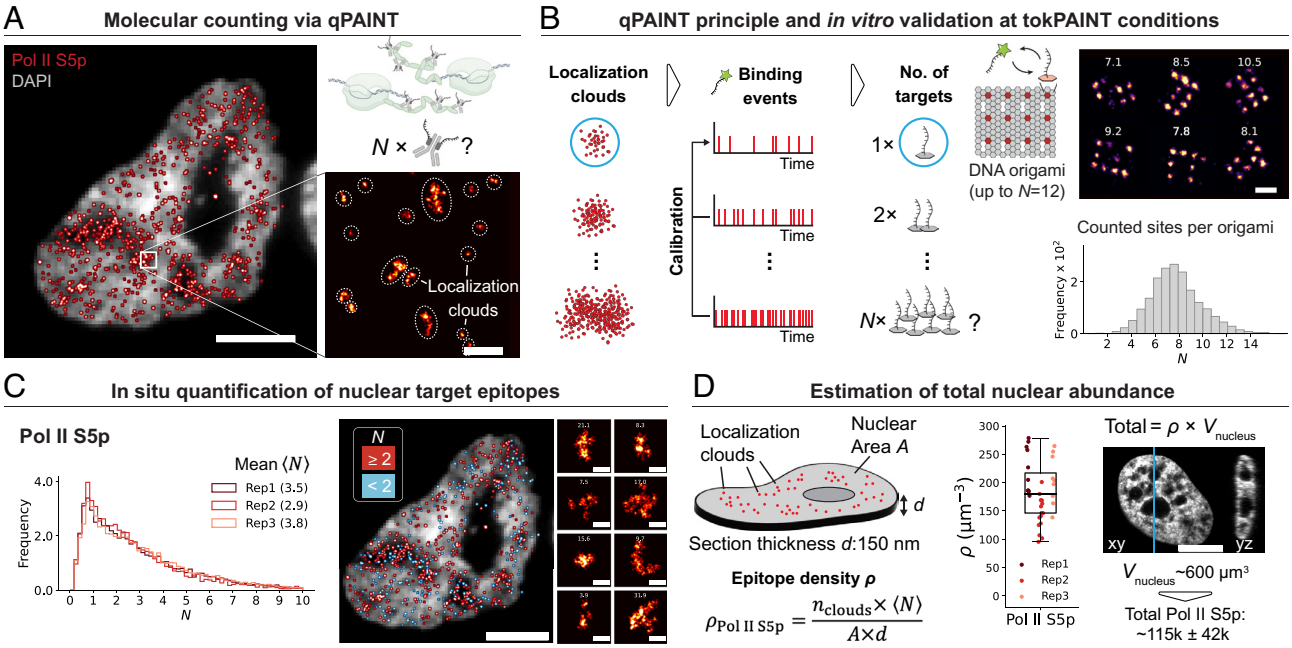

Fig. 3. Counting Pol II antibodies in nanoscopic complexes and total nuclear abundance. (*A*) tkPAINT Pol II S5p datasets contain heterogeneous localization clouds and qPAINT can be exploited to count antibody localization cloud. (*B*) Validating qPAINT using DNA origami imaged under tkPAINT conditions. *Left*: qPAINT principle (15). The smallest identifiable localization clouds, i.e., single docking strands on DNA origami (blue circle), serve as a calibration to measure the average imager binding frequency. Relative counting can be performed by comparing the binding frequency of each individual localization cloud to the calibration binding frequency. *Right*: Distribution of docking strand counts per DNA origami obtained via qPAINT analysis. *Right*: including six exemplary origami with their respective counting result stated above. (*C*) *Left*: Distribution of antibody counts per localization cloud for three Pol II S5p tkPAINT datasets obtained via qPAINT analysis. *Right*: image displayed in (*A*), rerendered by coloring localization clouds according to their antibody counts: red (≥2), blue (<2). The cutoff at 2 was chosen arbitrarily for illustration purposes. n = 3 replicates, each with ≥8,500 localization clouds from ≥10 cells. The small images on the *Right* show six exceptionally large localization clouds with antibody counts stated above. (*D*) Physical sectioning enables straightforward quantification of total nuclear target abundance by calculating the antibody density for the target epitope $\rho_{\text{Pol II S5p}}$ by knowing the number localization clouds, the average number of antibodies per localization cloud, the nuclear area, and the section thickness. $\rho_{\text{Pol II S5p}}$ for the three datasets in (*C*) is shown. Measuring the average nuclear volume of intact HeLa cells via confocal microscopy enables estimation of total nuclear abundance (x-y and x-z representation shown along the slice indicated by the blue line. The volume was averaged over n = 15 nuclei). Error bars and errors in (*D*) correspond to mean and SD. Scale bars, 3 µm in (*A*, *C*, and *D*), 100 nm in zoom-in in (*A*), and 40 nm in zoom-ins in (*B* and *D*).

the CTD of one or multiple Pol II molecules is present in a localization cloud; however, future studies using C-terminally tagged Pol II cell lines (71) could allow to address this question.

Finally, our data enabled us to assess the spatial distribution of Pol II S5p, which is known to associate with active chromatin or nuclear compartments, such as Pol II transcription factories and nuclear speckles, while being excluded from nucleoli (58, 59). Both nucleoli and nuclear speckles typically appear as regions of low intensity when staining DNA with DAPI. To confirm the identity of DAPI-weak compartments containing Pol II S5p, we performed costaining with the speckle marker SC35 (72) (*SI Appendix*, Fig. S14). These analyses show that regions with both low DAPI signal and Pol II S5p signal also colabeled with SC35, consistent with their identification as nuclear speckles. Accordingly, these regions exhibited both Pol II S5p higher antibody counts (Fig. 3*C*) and higher localization cloud densities as determined by nearest neighbor distance analysis (73) (*SI Appendix*, Fig. S14).

Resolution and Kinetic Enhancement Translate to tkPAINT Imaging in Mouse Tissues. Encouraged by successful applications of DNA-PAINT to semithin (~350 nm) Tokuyasu tissue sections (47, 48), we hypothesized that tkPAINT could also enable kinetic filtering, single-antibody resolution, and molecular counting in tissue samples. To test this, we prepared two mouse tissue types (cerebellum and spleen) following established protocols (74) (*Materials and Methods*) and processed 150 nm cryosections for tkPAINT tissue imaging of Pol II S5p, using R4-secondary nanobodies. Fig. 4*A* depicts superresolved tkPAINT images of Pol II S5p within cerebellum and spleen cryosections (two datasets were acquired per tissue type). As expected (47), we obtained similar localization precisions as previously in HeLa sections (~3 nm). The kinetic enhancement enabled by physical sectioning also translated to tissue imaging: ~55% of nuclear localizations could be assigned to repetitive localization clouds, confirming the suitability of tissue data for quantitative analysis (Fig. 4*B*). The lower kinetic filtering yield compared to HeLa (~70%) indicated slightly elevated sticking of R4 in both tissue types. We also performed center-of-mass alignments to obtain averaged sum images with decreasing minimum number of localizations per cloud to find the converging distribution width (*SI Appendix*, Fig. S15), further confirming tkPAINT's capability for single-antibody resolution in tissues (σ_{min} ≈ 3.4 nm and FWHM ≈ 8 nm; Fig. 4*C*).

Finally, we performed qPAINT analysis to obtain spatially resolved antibody counts in the nuclei of both tissue types

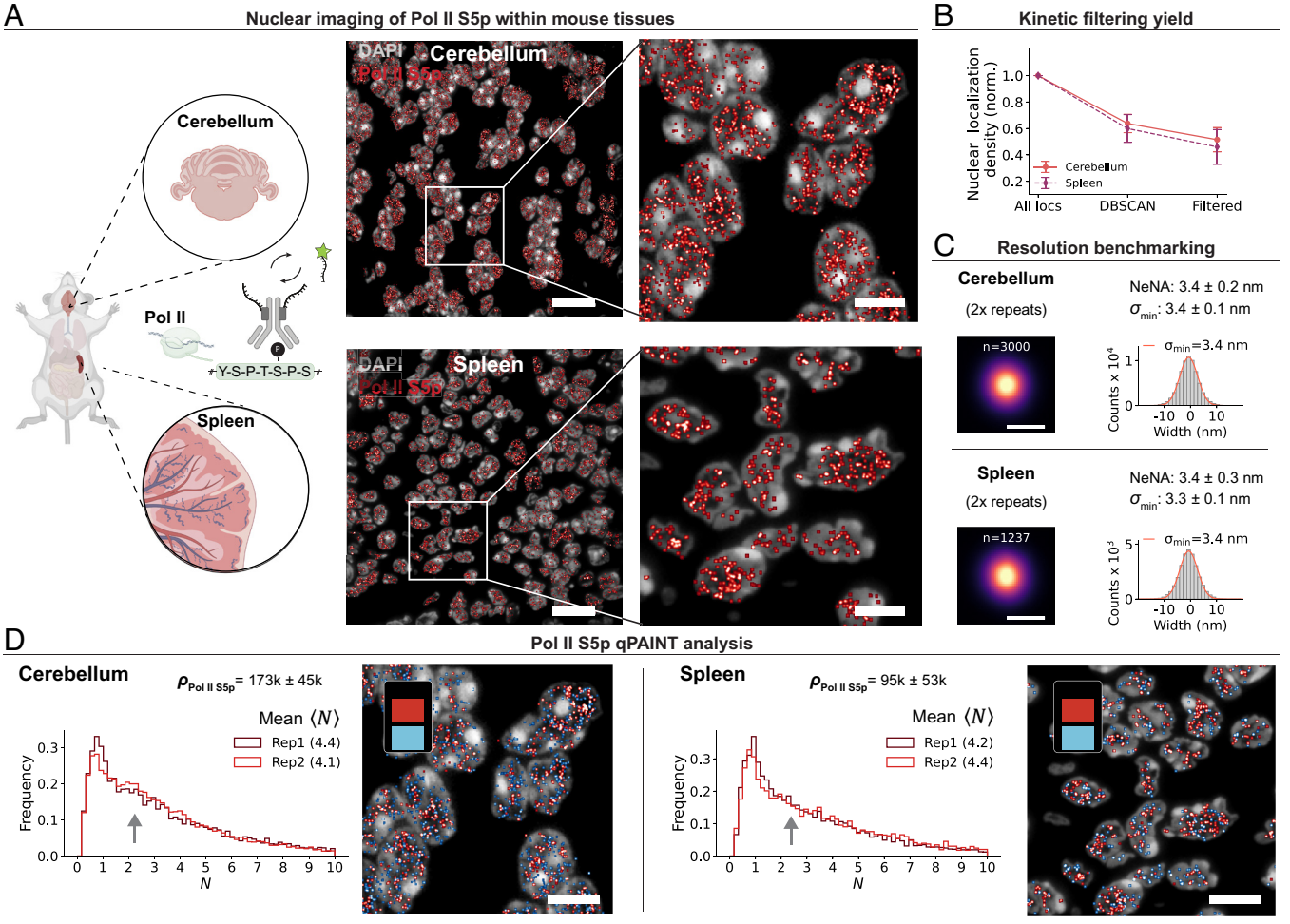

Fig. 4. Single-protein resolution and kinetic enhancement translate to tkPAINT tissue imaging. (*A*) Tissue blocks of mouse cerebellum and spleen were processed for Tokuyasu sectioning and subsequently stained for Pol II S5p prior to imaging. *Top*: tkPAINT image of region of mouse cerebellum and zoom-in to white box. *Bottom*: tkPAINT image of a region of mouse spleen and zoom-in to white box. (*B*) Kinetic filtering yield for cerebellum and spleen tkPAINT datasets. Normalized localization counts with respect to all nuclear localizations showing relative localization loss in each analysis step. n = 2 replicates per tissue type, each with ≥8,100 localization clouds from ≥46 cells. (*C*) Localization precision benchmarking for the cerebellum and spleen tkPAINT datasets from (*C*) (*Top* and *Bottom*, respectively). *Left*: rendered sum images of center-of-mass aligned localization clouds for one dataset each. *Right*: histograms showing the corresponding distribution of localizations fitted with a Gaussian (red curve) to obtain its SD σ_{min} (see *SI Appendix*, Fig. S11 for details and *SI Appendix*, Fig. S15 for all datasets). (*D*) qPAINT distributions showing number of Pol II S5p antibodies per localization cloud for cerebellum and spleen datasets. The antibody density $\rho_{Pol\ II\ S5p}$ is stated above. Error bars and errors in (*B–D*) correspond to mean and SD. Scale bars, 10 μm in (*A*), 5 μm in zoom-ins in (*A*), and 10 nm in (*C*).

(Fig. 4*D*). Each tissue yielded reproducible qPAINT distributions and averaged ~4.2 antibodies per localization cloud, higher than the ~3.2 observed in HeLa cells for the Pol II S5p epitope (Fig. 3*C*). Interestingly, while the qPAINT distribution for spleen closely matched that of HeLa cells, with a single-antibody peak and a long tail of higher antibody counts, the cerebellum datasets showed a second peak at ~2.5 antibodies (arrows, Fig. 4*D*). We observed a nearly twofold enriched average nuclear density in cerebellum nuclei (95 ± 53 μm^{-3} and 173 ± 45 μm^{-3}) and a higher cell-to-cell variability in spleen cells. These findings might reflect an intrinsic heterogeneity of transcriptional activity between tissue types and/or a higher number of cell types within the spleen (55, 56) (Fig. 4*D*). Furthermore, our results demonstrate that tkPAINT provides consistent imaging performance across diverse sample types and paves the way for probing molecular organizations between cultured cells and tissues.

Multiplexed and Multimodal tkPAINT for Nuclear Nanoscale Imaging in 2D and 3D. Next, we turned our attention toward several proof-of-concept demonstrations, showcasing the versatility of nuclear tkPAINT imaging with respect to multiplexed single-protein imaging. Circumventing use of any secondary label for Exchange-PAINT (47, 75), we conjugated primary antibodies targeting the nuclear lamina (Lamin A/C) and nuclear speckles (SC35), each with an orthogonal docking strand sequence in order to enable multiplexed imaging by sequential exchange of the complementary imager strands for each imaging round (Fig. 5*A*). Exchange-PAINT has the advantage of being free of chromatic aberrations since all imaging rounds can be acquired in the same color channel (9). Fig. 5*B* shows a multiplexed Exchange-tkPAINT image of Lamin A/C, Pol II S5p, and SC35, sequentially imaged and subsequently reconstructed using pseudocolors. Not only did sequential imaging enable us to perform quantitative analysis for all three nuclear antigens in parallel, it permitted the spatial probing of intermolecular relationships and features. *SI Appendix*, Fig. S16 provides examples on how multiplexed tkPAINT data can aid the study of nuclear organization. For instance, we observed two peaks in the distribution of nearest neighbor distances for Lamin A/C, which allowed us to separate the signal into a nucleoplasmic and lamina-association fraction (76, 77). Measuring nearest neighbor distances between Pol II S5p and SC35 aligned with the previously discussed spatial organization of Pol II S5p in and around nuclear speckles with SC35 at their center, as also observed with TSA-Seq (78). Given the surprisingly sparse SC35 signal, we wondered whether nonspecific DNA-conjugation of primary antibodies could affect their ability to bind their target epitope. Repeating the experiment with unlabeled primary antibodies and secondary

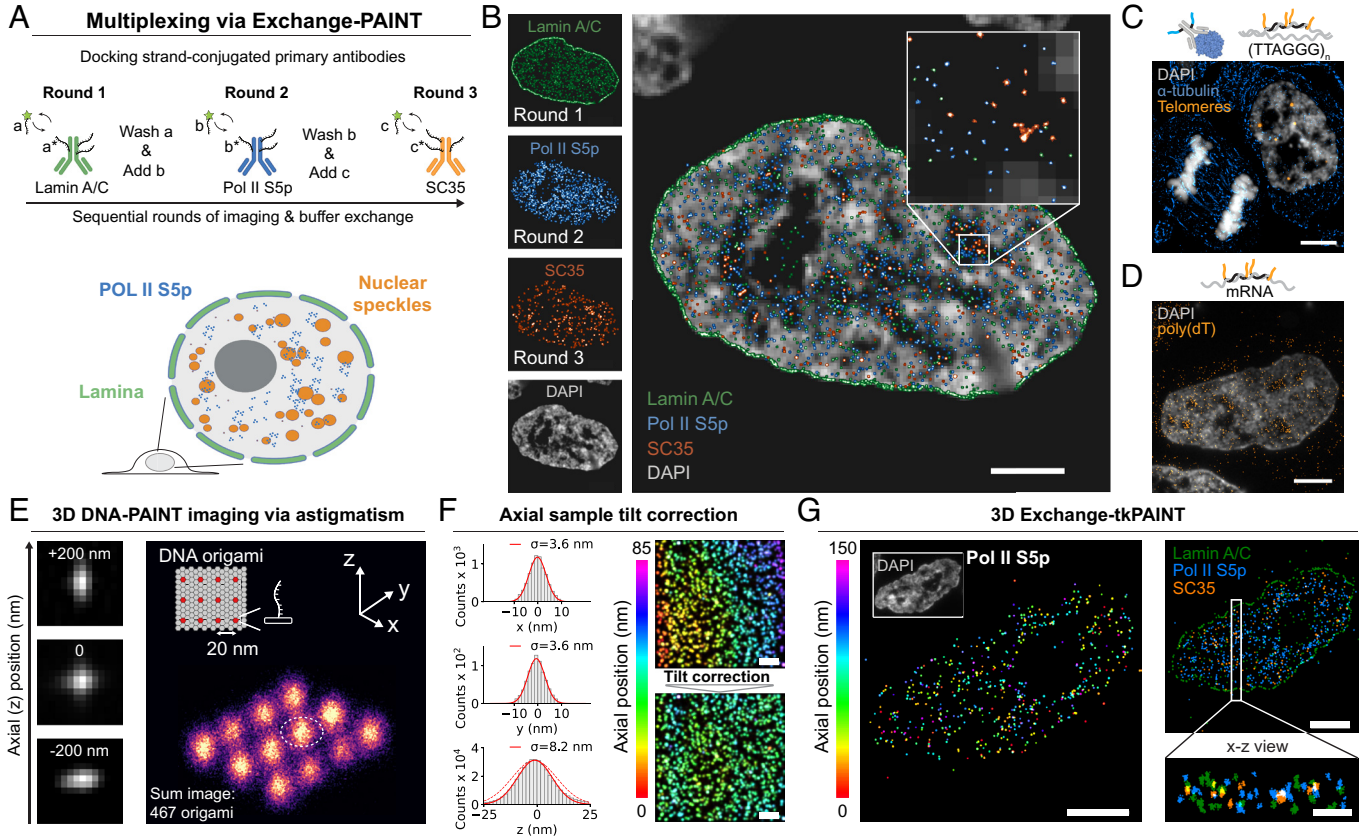

Fig. 5. Multiplexed and multimodal nuclear nanoscale imaging in 2D and 3D. (*A*) Schematic of Exchange-tkPAINT targeting Lamin A/C, Pol II S5p, and SC35. Primary antibodies are conjugated with orthogonal docking strands (sequences *a**, *b**, and *c**) and sequentially imaged with imager strands *a*, *b*, and *c*. Previous imager is washed out and subsequent imager is added between rounds of imaging. (*B*) Multiplexed tkPAINT image reconstructed from three rounds of sequential imaging. (*C*) Combined imaging of protein and DNA using tkPAINT targeting of α-tubulin and telomere repeats via FISH. (*D*) tkPAINT imaging of mRNA via poly(dT) hybridization probes. (*E*) Validation of cylindrical lens addition to a commercial TIRF system for 3D DNA-PAINT imaging. *Left*: Astigmatism-based encoding of axial position by reshaping the point spread function. *Right*: Sum DNA-PAINT image of 467 DNA origami with 20 nm docking strand pattern. (*F*) *Left*, *Top* and *Middle*: x and y line plot histograms across docking strand position indicated by white dashed circle in (*A*). *Left*, *Bottom*: Axial distribution of z coordinates of DNA origami dataset. The SD obtained by a Gaussian fit (red curve) is given above the histograms. *Right*: correction of axial sample tilt affecting measured z-distributions (red dashed curve in c). (*G*) *Left*: 3D tkPAINT of Pol II S5p. The color code indicates axial position of antibody signal over a range of 150 nm. *Right*: 3D Exchange-tkPAINT image of Lamin A/C (green), Pol II S5p (blue), and SC35 (orange). Side view (x-z) of localization clusters projected from white box. Scale bars, 5 μm in (*B*), 3 μm in (*C*), and 150 nm in zoom-in.

nanobodies reproduced the subnuclear pattern but indeed yielded denser speckle labeling (*SI Appendix*, Fig. S16). This highlights a need to evaluate antibody conjugation effects and a potential benefit of site-specific antibody conjugation strategies in future work (79).

Beyond multiplexed protein imaging, the same sections can be subject to both immunostaining and fluorescence in situ hybridization (80, 81), enabling analyses of the interplay between targeted proteins and specific sequences of RNA and/or DNA. Here, we performed proof-of-principle tkPAINT imaging of α-tubulin in cryosections that had additionally been labeled for telomeric repeats via in situ hybridization (Fig. 5*C*). Similarly, hybridization of a poly(dT) probe enabled us to perform tkPAINT imaging of mature mRNA (Fig. 5*D*).

TkPAINT data, previously generated through 2D imaging and, thus, resembling a 2D projection of molecules within cryosections, could be significantly enhanced by accessing the axial dimension for a true interrogation of nanoscale organization. To this end, we constructed a simple and affordable (~700$) custom addition to our commercial TIRF system that allowed us to insert a cylindrical lens in front of the camera for astigmatic 3D imaging (82) (*SI Appendix*, Fig. S17). We first benchmarked our 3D imaging capability, again using surface-immobilized DNA origami with 20-nm docking strand spacing. Although the docking strand arrangement, itself, was in 2D, it nevertheless allowed us to determine the achievable axial resolution in z as well as assess whether astigmatism would significantly reduce our lateral resolution. Fig. 5*E* shows an averaged 3D DNA-PAINT sum image of (~450 origami), demonstrating that individual docking strands could be laterally visualized at $FWHM_{x,y} \approx 8.5$ nm ($\sigma_{x,y} \approx 3.6$ nm), which was sufficient to resolve the 20-nm-spaced pattern (Fig. 5*F*). During DNA origami experiments, we observed that glass slides could be tilted with respect to the optical axis, as revealed when we colored localizations according to their axial position (Fig. 5*F*). To account for this tilt, we performed a z-correction by fitting and subtracting a 2D plane (83) (Fig. 5*F* and *SI Appendix*, Fig. S18). Post–tilt correction, 3D DNA-PAINT imaging of DNA origami yielded an axial distribution of localizations at $FWHM_z \approx 20$ nm ($\sigma_z \approx 8.5$ nm), in line with the known ~2× axial resolution drop for astigmatic 3D SMLM (82). An axial resolution of 20 nm would nevertheless allow us to determine distinct axial positions of antibodies within cryosections with a thickness of ~150 nm.

These validations enabled us to move on to 3D tkPAINT imaging within cryosections of fixed HeLa cells, repeating sequential imaging of Lamin A/C, Pol II S5p, and SC35 (Fig. 5*G*). The left image in Fig. 5*G* shows the superresolved Pol II S5p image rendered with a range of colors according to the z-position of each localization over an axial range of 150 nm. It has been shown that, for unpermeabilized cryosections, antibody labeling happens predominantly at both surfaces of sections (84). However, the permeabilization step in our protocol ensured antibody penetration throughout the sections, as seen for both localization clouds of all colors in the Pol II S5p image alone and the x-z projection of the multicolor Exchange-tkPAINT image (Fig. 5 *G*, *Left* and *Right*, respectively; see also *SI Appendix*, Fig. S19). Overall, our 3D tkPAINT results are in close agreement with the cryotome setting for a cutting thickness of 150 nm. Measuring the overall z-distributions, we observed that while Lamin A/C and Pol II S5p labeling penetrated more homogeneously, SC35 exhibited stronger staining toward the top half of the section (*SI Appendix*, Fig. S19). While these proof-of-concept results demonstrate the capability of 3D tkPAINT for assessing section labeling, additional controls would be required to determine whether this label penetration variability really is systematic. Smaller labels such as primary nanobodies, adjusted section permeabilization or varied section thickness could promote homogeneous labeling.

Discussion

With tkPAINT, we used ultrathin sectioning to align sample volume with TIRF illumination, maximizing the capability of DNA-PAINT for single-protein imaging and counting across diverse samples and molecular targets. By leveraging the Tokuyasu method (46), we overcame the range constraint of TIRF to access distal intracellular regions (33), such as the nucleus, and demonstrated tkPAINT imaging throughout ultrastructure-preserved HeLa cells down to 3 nm localization precision. For imaging nuclear antigens such as Pol II S5p, this enabled up to threefold improved localization precisions as compared to HILO imaging in whole cells. Physical sectioning decrowded the sample volume, improving imager binding statistics critical for robust single-protein imaging (13, 14) and counting (15, 67) as well as accelerating image acquisition. This allowed us to count S5p antibodies within nanoscopic Pol II clusters as well as to quantify cell- and tissue-specific heterogeneities in Pol II organization. Additionally, sequential multiplexing (9) facilitated combined imaging of proteins and nucleic acids, while astigmatism-based axial encoding (82) enabled imaging in 3D.

TkPAINT holds significant potential for advancing multiplexing strategies for spatial proteomics with DNA-PAINT. Current sequential DNA-PAINT schemes have achieved up to 30-plex imaging (10, 11). Single-antibody resolution in tkPAINT could enable incorporation of barcoding (85–87) or in situ sequencing (88–90) approaches, potentially scaling to hundreds of targets in fewer rounds. Computational methods (91, 92) and isotropic 3D imaging (93–96) could further refine axial encoding. Additionally, tkPAINT could be combined with RESI (14) to reach Ångstrom resolution or complement nanoscopy approaches such as MINFLUX (97), particularly for dense compartments such as the nucleus. Finally, parallel sample preparation could offer unique opportunities for correlative super-resolution and electron microscopy (34, 40, 98, 99), further broadening tkPAINT's versatility.

Limitations of our study include the steric hindrance, imperfect labeling efficiency, and variability in specificity inherent to antibody labeling, which only serves as a proxy for the true molecular distribution. Smaller, stoichiometric labels (one docking strand per target), such as primary nanobodies (100), genetic tags (101), or unnatural amino acids (102), could address these challenges, improving both structural resolution and molecular quantifications (70). High-pressure freezing and freeze substitution (103, 104) offer a promising route to further minimize fixation artifacts and capture molecular organization closer to the in vivo state (20, 49). However, accessibility trade-offs between certain antigens also apply to sections—for example, microtubule labeling is often enhanced by glutaraldehyde fixation and a commonly used detergent-based pre-extraction step prior to fixation (105), at the cost of ultrastructural loss of other cytoplasmic components and reduced detectability of glutaraldehyde-sensitive antigens.

The reduced imaging volume of tkPAINT compared to whole-cell imaging limits visualization of low-abundance targets and larger structures such as entire genomic regions (54). Furthermore, compartments such as larger nuclear speckles might appear as multiple smaller structures in a single section. Serial cryosectioning (32, 40, 106) could address this but would require optimization in order to mitigate challenges such as partial sample loss and folding during manual handling. Combining ultramicrotomy with resin embedding as in array tomography (45, 57) may provide an alternative, though at reduced antigenicity (35). Implementation

of machine learning (48, 107, 108) and automated imager exchange (44) could accelerate tkPAINT imaging to promote volumetric reconstructions. Nevertheless, the strong potential for studying molecular principles of genome organization in single sections is highlighted by the wealth of information gained from super-resolution studies that are based on single nuclear "optical sections," often in 2D: Recent examples include local chromatin compaction, in situ mapping of epigenetic marks, nucleosome clustering, the nanoscale arrangement of master regulator proteins such as cohesin and CTCF, or the structural biomolecular composition (proteins, RNA) of nuclear compartments such as nucleoli or paraspeckles (51–53, 109–115).

Our work enhances the potential of DNA-PAINT for single-protein imaging in various aspects. Through sectioning, we decoupled imaging performance from target selection, achieving optimal conditions for probing nanoscale organization even in dense intracellular environments. Unlike whole-cell nuclear immunolabeling, which requires disruptive permeabilization (19), tkPAINT leverages permeabilization-free access to the nucleus in ultrastructure-preserved cells. This unique feature could enable functional studies linking nuclear and cytoplasmic mechanisms. The integration of in situ hybridization with immunolabeling extends this potential for multimodal investigations of protein–nucleic acid interactions. Finally, consistent imaging performance in both cultured cells and tissues demonstrates tkPAINT's potential for comparative studies between cultured cells and tissues. In conclusion, we believe tkPAINT's broad applicability will help drive DNA-PAINT toward becoming a routine tool for biological discovery.

Materials and Methods

Please refer to the *SI Appendix* for a detailed explanation of all materials and methods. In summary, unmodified, dye-labeled, and modified DNA oligonucleotides, antibodies/nanobodies, chambered glass slides, enzymes, and standard reagents (buffers, fixatives, fiducials, oxygen scavengers) were purchased from commercial suppliers. Antibodies and nanobodies were in-house conjugated to azide-modified DNA docking strands using DBCO-sulfo-NHS chemistry. Pellets of PFA-fixed HeLa cells and mouse tissues (1 to 2 mm^3) were infiltrated with high molarity sucrose for cryopreservation, frozen in liquid nitrogen, and cryosectioned according to the Tokuyasu method (46). Cryosections were collected using drops of sucrose-methyl cellulose solution and placed on glow-discharged glass slides, immunolabeled, and imaged using a Nikon Ti TIRF microscope (sCMOS, 100× objective, optional 3D via astigmatism). A direct comparison between tkPAINT imaging of cryosections and conventional HILO imaging of fixed whole cells was conducted to evaluate improvements with respect to localization precision and binding kinetics. DNA origami nanostructures were folded in house and imaged as reference targets. All data were processed with Picasso (8), Fiji (116), and custom Python modules (16, 117).

Data, Materials, and Software Availability. Single-molecule localization microscopy, fluorescence microscopy, and electron microscopy data generated in this study have been deposited in a Zenodo database: https://doi.org/10.5281/zenodo.16411486 (118).

ACKNOWLEDGMENTS. We thank Paula Montero Llopis and Praju Vikas Anekal at Harvard Medical School (HMS) MicRoN Imaging Facility, Margaret Coughlin and Anja Nordstrom at HMS Electron Microscopy Core, and Tom Ferrante, Maurice Perez, and Talley Lambert for valuable experimental support. We thank Miiko Sokka and Nicola Neretti for sharing and providing antibodies on short notice and for helpful discussions. We thank Oliver Dodd and Soufiane Aboulhouda for sharing mouse tissues. We thank Robert Tjian, Thomas Graham, Claudia Cattoglio, and Nam Che for sharing cell lines and plasmids as well as Merrick Pierson Smela for help regarding plasmid recovery and transfection. We thank Silvia Filipa Carvalho and Izabela-Cezara Harabula for sharing protocols and discussing Tokuyasu cryosectioning for fluorescence microscopy. We thank the Bewersdorf lab at Yale University for sharing fluorogenic imagers and docking strand-conjugated secondary antibodies. We thank Gareth Griffiths and Heinz Schwarz for helpful discussions and invaluable expert advice regarding the Tokuyasu-Method. We thank Nuno Martins, Fei Zhao, Antonios Lioutas, Jumana Alhaj Abed, Tae Ryu, Eunice Fabian-Morales, and Erkin Kuru for manuscript feedback and helpful discussions. We further acknowledge helpful discussions with Hylkje Geertsema, Yolanda Markaki, Bas van Steensel, Merle Hantsche-Grininger, Peter Becker, Christophe Leterrier, and Hiroshi Sasaki. We acknowledge biorender.com which was partially used in the illustrations. J.S. acknowledges support by the European Molecular Biology Organization (ALTF 816-2021). R.B.M. acknowledges support by NSF (Graduate Research Fellowship grant 2140743) and NIH (Molecular Biophysics Training grant NIGMS T32 GM008313). P.Y. acknowledges support by the NIH (Pioneer Award DP1GM133052). A.P. acknowledges support by the Helmholtz Association. G.M.C. acknowledges support by the Department of Energy (DE-FG02-02ER63445). C.-t.W. acknowledges funding from NIH (4D Nucleome Program 5RM1HG011016-03 and 5UM1HG011593).

Author affiliations: [a]Wyss Institute of Biologically Inspired Engineering, Boston, MA 02115; [b]Department of Genetics, Harvard Medical School, Boston, MA 02115; [c]Blavatnik Institute, Harvard Medical School, Boston, MA 02115; [d]Max-Delbrück-Center for Molecular Medicine in the Helmholtz Association, Berlin Institute for Medical Systems Biology, Epigenetic Regulation and Chromatin Architecture Group, Berlin 10115, Germany; [e]Humboldt-Universität zu Berlin, Institute for Biology, Berlin 10117, Germany; and [f]Department of Biosciences, University of Oslo, Oslo 0316, Norway

Author contributions: J.S., G.M.C., and C.-t.W. designed research; J.S., M.E., L.M., and S.A. performed research; J.S., M.N., R.B.M., L.B., C.P.H., S.D.L., A.W., J.W., L.A.-J., P.Y., and A.P. contributed new reagents/analytic tools; J.S., L.B., and J.W. analyzed data; and J.S., M.N., A.P., G.M.C., and C.-t.W. wrote the paper.

Competing interest statement: G.M.C. is a scientific advisor to 10× Genomics and holds equity in the company. C.-t.W. holds or has patent filings pertaining to imaging, and her laboratory has held a sponsored research agreement with Bruker Inc. C.-t.W. is a co-founder of Acuity Spatial Genomics and, through personal connections to G.M.C., has equity in companies associated with him, including 10× Genomics and Twist. A.P. holds a patent on "Genome Architecture Mapping." P.Y. is also a co-founder, equity holder, director and consultant of Ultivue, Inc. and Digital Biology, Inc. All other authors declare no competing financial interest.

1. K. Vandereyken, A. Sifrim, B. Thienpont, T. Voet, Methods and applications for single-cell and spatial multi-omics. *Nat. Rev. Genet.* **24**, 494–515 (2023).
2. J. Dekker *et al.*, Spatial and temporal organization of the genome: Current state and future aims of the 4D nucleome project. *Mol. Cell* **83**, 2624–2640 (2023).
3. A. Rao, D. Barkley, G. S. França, I. Yanai, Exploring tissue architecture using spatial transcriptomics. *Nature* 596, 211–220 (2021).
4. S. J. Sahl, S. W. Hell, S. Jakobs, Fluorescence nanoscopy in cell biology. *Nat. Rev. Mol. Cell Biol.* 18, 685–701 (2017).
5. M. Sauer, M. Heilemann, Single-molecule localization microscopy in eukaryotes. *Chem. Rev.* **117**, 7478–7509 (2017).
6. M. Lelek *et al.*, Single-molecule localization microscopy. *Nat. Rev. Methods Primers* **1**, 1–27 (2021).
7. V. Flores, I. Farabella, G. Nir, Genome-wide tracing to decipher nuclear organization. *Curr. Opin. Cell Biol.* **82**, 102175 (2023).
8. J. Schnitzbauer, M. T. Strauss, T. Schlichthaerle, F. Schueder, R. Jungmann, Super-resolution microscopy with DNA-PAINT. *Nat. Protoc.* **12**, 1198 (2017).
9. R. Jungmann *et al.*, Multiplexed 3D cellular super-resolution imaging with DNA-PAINT and Exchange-PAINT. *Nat. Methods* **11**, 313–318 (2014).
10. E. M. Unterauer *et al.*, Spatial proteomics in neurons at single-protein resolution. *Cell* **187**, 1785–1800.e16 (2024).
11. F. Schueder *et al.*, Unraveling cellular complexity with transient adapters in highly multiplexed super-resolution imaging. *Cell* **187**, 1769–1784.e18 (2024).
12. S. Strauss *et al.*, Modified aptamers enable quantitative sub-10-nm cellular DNA-PAINT imaging. *Nat. Methods* **15**, 685–688 (2018).
13. L. S. Fischer *et al.*, Quantitative single-protein imaging reveals molecular complex formation of integrin, talin, and kindlin during cell adhesion. *Nat. Commun.* **12**, 919 (2021).
14. S. C. M. Reinhardt *et al.*, Ångström-resolution fluorescence microscopy. *Nature* **617**, 711–716 (2023).
15. R. Jungmann *et al.*, Quantitative super-resolution imaging with qPAINT. *Nat. Methods* **13**, 439 (2016).
16. J. Stein, F. Stehr, R. Jungmann, P. Schwille, Calibration-free counting of low molecular copy numbers in single DNA-PAINT localization clusters. *Biophys. Rep.* **1**, 100032 (2021).
17. G. Griffiths, *Fine Structure Immunocytochemistry* (Springer Berlin Heidelberg, 1993).
18. U. Schnell, F. Dijk, K. A. Sjollema, B. N. G. Giepmans, Immunolabeling artifacts and the need for live-cell imaging. *Nat. Methods* **9**, 152–158 (2012).
19. B. M. Humbel, M. D. M. de Jong, W. H. Müller, A. J. Verkleij, Pre-embedding immunolabeling for electron microscopy: An evaluation of permeabilization methods and markers. *Microsc. Res. Tech.* **42**, 43–58 (1998).
20. S. Irgen-Gioro, S. Yoshida, V. Walling, S. Chong, Fixation can change the appearance of phase separation in living cells. *Elife* **11**, e79903 (2022).
21. K. A. K. Tanaka *et al.*, Membrane molecules mobile even after chemical fixation. *Nat. Methods* **7**, 865–866 (2010).
22. F. Schueder *et al.*, Multiplexed 3D super-resolution imaging of whole cells using spinning disk confocal microscopy and DNA-PAINT. *Nat. Commun.* **8**, 2090 (2017).

23. A. Ghosh, M. Meub, D. A. Helmerich, S. Doose, M. Sauer, Fast, whole-cell DNA-PAINT imaging with dual-labeled self-quenched imager probes. bioRxiv [Preprint] (2023). https://doi.org/10.1101/2023.10.09.561472 (Accessed 18 June 2024).
24. D. Axelrod, Cell-substrate contacts illuminated by total internal reflection fluorescence. *J. Cell Biol.* **89**, 141–145 (1981).
25. C. Böger *et al.*, Super-resolution imaging and estimation of protein copy numbers at single synapses with DNA-point accumulation for imaging in nanoscale topography. *Neurophotonics* **6**, 035008 (2019).
26. K. Huang *et al.*, Quantitative, super-resolution localization of small RNAs with sRNA-PAINT. *Nucleic Acids Res.* **48**, E96 (2020).
27. L. F. Marcano-García *et al.*, Quantitative analysis of protein-protein equilibrium constants in cellular environments using single-molecule localization microscopy. *Nano Lett.* **24**, 13834–13842 (2024), 10.1021/acs.nanolett.4c04394.
28. I. Jayasinghe *et al.*, True molecular scale visualization of variable clustering properties of Ryanodine receptors. *Cell Rep.* **22**, 557–567 (2018).
29. B. Geiger, K. T. Tokuyasu, S. J. Singer, Immunocytochemical localization of alpha-actinin in intestinal epithelial cells. *Proc. Natl. Acad. Sci. U.S.A.* **76**, 2833–2837 (1979).
30. A. Pombo, M. Hollinshead, P. R. Cook, Bridging the resolution gap: Imaging the same transcription factories in cryosections by light and electron microscopy. *J. Histochem. Cytochem.* **47**, 471–480 (1999).
31. H. Schwarz, B. M. Humbel, "Correlative light and electron microscopy using immunolabeled resin sections" in *Electron Microscopy: Methods and Protocols*, J. Kuo, Ed. (*Methods in Molecular Biology*, Humana Press 2, 2007), pp. 229–256.
32. G. Vicidomini *et al.*, High data output and automated 3D correlative light-electron microscopy method. *Traffic* **9**, 1828–1838 (2008).
33. E. Betzig *et al.*, Imaging intracellular fluorescent proteins at nanometer resolution. *Science* **313**, 1642–1645 (2006).
34. B. G. Kopek *et al.*, Diverse protocols for correlative super-resolution fluorescence imaging and electron microscopy of chemically fixed samples. *Nat. Protoc.* **12**, 916–946 (2017).
35. W. Möbius, G. Posthuma, Sugar and ice: Immunoelectron microscopy using cryosections according to the Tokuyasu method. *Tissue Cell* **57**, 90–102 (2019).
36. S. Nanguneri, B. Flottmann, H. Horstmann, M. Heilemann, T. Kuner, Three-dimensional, tomographic super-resolution fluorescence imaging of serially sectioned thick samples. *PLoS One* **7**, e38098 (2012).
37. B. G. Kopek, G. Shtengel, C. S. Xu, D. A. Clayton, H. F. Hess, Correlative 3D superresolution fluorescence and electron microscopy reveal the relationship of mitochondrial nucleoids to membranes. *Proc. Natl. Acad. Sci. U.S.A.* 109, 6136–6141 (2012).
38. M. Perkovic *et al.*, Correlative light- and electron microscopy with chemical tags. *J. Struct. Biol.* **186**, 205–213 (2014).
39. Y. M. Sigal, C. M. Speer, H. P. Babcock, X. Zhuang, Mapping synaptic input fields of neurons with super-resolution imaging. *Cell* **163**, 493–505 (2015).
40. C. Franke *et al.*, Correlative single-molecule localization microscopy and electron tomography reveals endosome nanoscale domains. *Traffic* **20**, 601–617 (2019).
41. Y. Wang *et al.*, Rapid sequential in situ multiplexing with DNA exchange imaging in neuronal cells and tissues. *Nano Lett.* **17**, 6131–6139 (2017).
42. S. Park *et al.*, Superresolution fluorescence microscopy for 3D reconstruction of thick samples. *Mol. Brain* **11**, 17 (2018).
43. A. H. Clowsley *et al.*, Repeat DNA-PAINT suppresses background and non-specific signals in optical nanoscopy. *Nat. Commun.* **12**, 1–10 (2021).
44. M. J. Rames *et al.*, Multiplexed and millimeter-scale fluorescence nanoscopy of cells and tissue sections via prism-illumination and microfluidics-enhanced DNA-PAINT. *Chem. Biomed. Imaging* **1**, 817–830 (2023), 10.1021/cbmi.3c00060.
45. M. Colom-Cadena *et al.*, Synaptic oligomeric tau in Alzheimer's disease–A potential culprit in the spread of tau pathology through the brain. *Neuron* **111**, 2170–2183.e6 (2023).
46. K. T. Tokuyasu, A technique for ultracryotomy of cell suspensions and tissues. *J. Cell Biol.* **57**, 551–565 (1973).
47. K. K. Narayanasamy *et al.*, Visualizing synaptic multi-protein patterns of neuronal tissue with DNA-assisted single-molecule localization microscopy. *Front. Synaptic Neurosci.* **13**, 671288 (2021).
48. K. K. Narayanasamy, J. V. Rahm, S. Tourani, M. Heilemann, Fast DNA-PAINT imaging using a deep neural network. *Nat. Commun.* **13**, 5047 (2022).
49. P. V. Guillot, S. Q. Xie, M. Hollinshead, A. Pombo, Fixation-induced redistribution of hyperphosphorylated RNA polymerase II in the nucleus of human cells. *Exp. Cell Res.* **295**, 460–468 (2004).
50. B. J. Beliveau *et al.*, "In situ super-resolution imaging of genomic DNA with oligoSTORM and oligoDNA-PAINT" in *Methods in Molecular Biology,* H. Erfle, Ed. (Humana Press Inc., 2017), pp. 231–252.
51. J. Otterstrom *et al.*, Super-resolution microscopy reveals how histone tail acetylation affects DNA compaction within nucleosomes in vivo. *Nucleic Acids Res.* **47**, 8470–8484 (2019).
52. A. Castells-Garcia *et al.*, Super resolution microscopy reveals how elongating RNA polymerase II and nascent RNA interact with nucleosome clutches. *Nucleic Acids Res.* **50**, 175–190 (2022).
53. F. Frottin *et al.*, The nucleolus functions as a phase-separated protein quality control compartment. *Science* **365**, 342–347 (2019).
54. H. M. Sasaki, J. Y. Kishi, C. Wu, B. J. Beliveau, P. Yin, Quantitative multiplexed imaging of chromatin ultrastructure with Decode-PAINT. bioRxiv [Preprint] (2022). https://doi.org/10.1101/2022.08.01.502089 (Accessed 7 February 2025).
55. E. Lein, L. E. Borm, S. Linnarsson, The promise of spatial transcriptomics for neuroscience in the era of molecular cell typing. *Science* **358**, 64–69 (2017).
56. S. K. Longo, M. G. Guo, A. L. Ji, P. A. Khavari, Integrating single-cell and spatial transcriptomics to elucidate intercellular tissue dynamics. *Nat. Rev. Genet.* 22, 627–644 (2021).
57. K. D. Micheva, S. J. Smith, Array tomography: A new tool for imaging the molecular architecture and ultrastructure of neural circuits. *Neuron* **55**, 25–36 (2007).
58. H. Kimura, Y. Sato, Imaging transcription elongation dynamics by new technologies unveils the organization of initiation and elongation in transcription factories. *Curr. Opin. Cell Biol.* **74**, 71–79 (2022).
59. S. Q. Xie, S. Martin, P. V. Guillot, D. L. Bentley, A. Pombo, Splicing speckles are not reservoirs of RNA polymerase II, but contain an inactive form, phosphorylated on serine2 residues of the C-terminal domain. *Mol. Biol. Cell* **17**, 1723–1733 (2006).
60. S. Strauss, R. Jungmann, Up to 100-fold speed-up and multiplexing in optimized DNA-PAINT. *Nat. Methods* **17**, 1–3 (2020).
61. U. Endesfelder, S. Malkusch, F. Fricke, M. Heilemann, A simple method to estimate the average localization precision of a single-molecule localization microscopy experiment. *Histochem. Cell Biol.* **141**, 629–638 (2014).
62. K. K. H. Chung *et al.*, Fluorogenic DNA-PAINT for faster, low-background super-resolution imaging. *Nat. Methods* **19**, 554–559 (2022), 10.1038/s41592-022-01464-9.
63. P. W. K. Rothemund, Folding DNA to create nanoscale shapes and patterns. *Nature* **440**, 297 (2006).
64. C. Bond, S. Hugelier, J. Xing, E. M. Sorokina, M. Lakadamyali, Heterogeneity of late endosome/lysosomes shown by multiplexed DNA-PAINT imaging. *J. Cell Biol.* **224**, e202403116 (2024).
65. M. R. Branco, S. Q. Xie, S. Martin, A. Pombo, "Correlative microscopy using Tokuyasu cryosections: Applications for immunogold labelling and in situ hybridisation" in *Cell Imaging (Methods Express Series),* D. Stephens, Ed. (Scion Publishing, 2006), pp. 201–217.
66. O. K. Wade *et al.*, 124-color super-resolution imaging by engineering DNA-PAINT blinking kinetics. *Nano Lett.* **19**, 2641–2646 (2019).
67. J. Stein *et al.*, Toward absolute molecular numbers in DNA-PAINT. *Nano Lett.* **19**, 8182–8190 (2019).
68. M. Ester, H.-P. Kriegel, J. Sander, X. Xu, "A density-based algorithm for discovering clusters in large spatial databases with noise" in *Proceedings of the 2nd International Conference on Knowledge Discovery and Data Mining,* E. Simoudis, J. Han, U. Fayyad, Eds. (AAAI Press, 1996), pp. 226–231.
69. F. Schueder *et al.*, An order of magnitude faster DNA-PAINT imaging by optimized sequence design and buffer conditions. *Nat. Methods* **16**, 1101–1104 (2019).
70. S. Liu, P. Hoess, J. Ries, Super-resolution microscopy for structural cell biology. *Annu. Rev. Biophys.* **51**, 301–326 (2022).
71. M. Boehning *et al.*, RNA polymerase II clustering through carboxy-terminal domain phase separation. *Nat. Struct. Mol. Biol.* **25**, 833–840 (2018).
72. İA. Ilik *et al.*, SON and SRRM2 are essential for nuclear speckle formation. *Elife* **9**, e60579 (2020).
73. J. Kim, N. C. Venkata, G. A. Hernandez Gonzalez, N. Khanna, A. S. Belmont, Gene expression amplification by nuclear speckle association. *J. Cell Biol.* **219**, e201904046 (2019).
74. S. Q. Xie, L. M. Lavitas, A. Pombo, CryoFISH: Fluorescence in situ hybridization on ultrathin cryosections. *Methods Mol. Biol.* **659**, 219–230 (2010).
75. S. S. Agasti *et al.*, DNA-barcoded labeling probes for highly multiplexed exchange-PAINT imaging. *Chem. Sci.* **8**, 3080–3091 (2017).
76. T. Dechat *et al.*, Nuclear lamins: Major factors in the structural organization and function of the nucleus and chromatin. *Genes Dev.* **22**, 832–853 (2008).
77. K. Ikegami, S. Secchia, O. Almakki, J. D. Lieb, I. P. Moskowitz, Phosphorylated lamin A/C in the nuclear interior binds active enhancers associated with abnormal transcription in progeria. *Dev. Cell* **52**, 699–713.e11 (2020).
78. Y. Chen *et al.*, Mapping 3D genome organization relative to nuclear compartments using TSA-seq as a cytological ruler. *J. Cell Biol.* **217**, 4025–4048 (2018).
79. J. Hellmeier *et al.*, Quantification of absolute labeling efficiency at the single-protein level. *Nat. Methods* **21**, 1702–1707 (2024), 10.1038/s41592-024-02242-5.
80. M. R. Branco, A. Pombo, Intermingling of chromosome territories in interphase suggests role in translocations and transcription-dependent associations. *PLoS Biol.* **4**, e138 (2006).
81. C. Ferrai *et al.*, Poised transcription factories prime silent uPA gene prior to activation. *PLoS Biol.* **8**, e1000270 (2010).
82. B. Huang, W. Wang, M. Bates, X. Zhuang, Three-dimensional super-resolution imaging by stochastic optical reconstruction microscopy. *Science* **319**, 810–813 (2008).
83. C. Franke *et al.*, Approach to map nanotopography of cell surface receptors. *Commun. Biol.* **5**, 1–16 (2022).
84. Y.-D. Stierhof, H. Schwarz, H. Frank, Transverse sectioning of plastic-embedded immunolabeled cryosections: Morphology and permeability to protein A-colloidal gold complexes. *J. Ultrastruct. Mol. Struct. Res.* **97**, 187–196 (1986).
85. B. J. Beliveau *et al.*, Versatile design and synthesis platform for visualizing genomes with Oligopaint FISH probes. *Proc. Natl. Acad. Sci U.S.A.* **109**, 21301–21306 (2012).
86. K. H. Chen, A. N. Boettiger, J. R. Moffitt, S. Wang, X. Zhuang, Spatially resolved, highly multiplexed RNA profiling in single cells. *Science* **348**, aaa6090 (2015).
87. C. H. L. Eng *et al.*, Transcriptome-scale super-resolved imaging in tissues by RNA seqFISH+. *Nature* **568**, 235–239 (2019).
88. J. H. Lee *et al.*, Highly multiplexed subcellular RNA sequencing in situ. *Science* **343**, 1360–1363 (2014).
89. H. Q. Nguyen *et al.*, 3D mapping and accelerated super-resolution imaging of the human genome using in situ sequencing. *Nat. Methods* **17**, 822–832 (2020).
90. R. E. Kohman, G. M. Church, Fluorescent in situ sequencing of DNA barcoded antibodies. bioRxiv [Preprint] (2020). https://doi.org/10.1101/2020.04.27.060624 (Accessed 5 March 2021).
91. Y. Li *et al.*, Real-time 3D single-molecule localization using experimental point spread functions. *Nat. Methods* **15**, 367 (2018).
92. S. Fu *et al.*, Field-dependent deep learning enables high-throughput whole-cell 3D super-resolution imaging. *Nat. Methods* **20**, 459–468 (2023).
93. J. C. Thiele *et al.*, Isotropic three-dimensional dual-color super-resolution microscopy with metal-induced energy transfer. *Sci. Adv.* **8**, eabo2506 (2022).
94. F. Huang *et al.*, Ultra-high resolution 3d imaging of whole cells. *Cell* **166**, 1028–1040 (2016).
95. G. Shtengel *et al.*, Interferometric fluorescent super-resolution microscopy resolves 3D cellular ultrastructure. *Proc. Natl. Acad. Sci. U.S.A.* **106**, 3125–3130 (2009).
96. M. Bates *et al.*, Optimal precision and accuracy in 4Pi-STORM using dynamic spline PSF models. *Nat. Methods* **19**, 603–612 (2022).
97. F. Balzarotti *et al.*, Nanometer resolution imaging and tracking of fluorescent molecules with minimal photon fluxes. *Science* **355**, 606–612 (2017).
98. D. M. van Elsland *et al.*, Ultrastructural imaging of Salmonella-host interactions using super-resolution correlative light-electron microscopy of bioorthogonal pathogens. *Chembiochem* **19**, 1766–1770 (2018).
99. J. Beek, C. Heus, N. Liv, J. Klumperman, Quantitative correlative microscopy reveals the ultrastructural distribution of endogenous endosomal proteins. *J. Cell Biol.* **221**, e202106044 (2021).
100. S. Sograte-Idrissi *et al.*, Nanobody detection of standard fluorescent proteins enables multi-target DNA-PAINT with high resolution and minimal displacement errors. *Cells* **8**, 48 (2019).
101. H. Götzke *et al.*, The ALFA-tag is a highly versatile tool for nanobody-based bioscience applications. *Nat. Commun.* **10**, 4403 (2019).
102. A. Kuhlemann *et al.*, Genetic code expansion and click-chemistry labeling to visualize GABA-A receptors by super-resolution microscopy. *Front. Synaptic Neurosci.* **13**, 727406 (2021).

103. E. van Donselaar, G. Posthuma, D. Zeuschner, B. M. Humbel, J. W. Slot, Immunogold labeling of cryosections from high-pressure frozen cells. *Traffic* **8**, 471–485 (2007).
104. E. D'Este, G. Lukinavičius, R. Lincoln, F. Opazo, E. F. Fornasiero, Advancing cell biology with nanoscale fluorescence imaging: Essential practical considerations. *Trends Cell Biol.* **34**, 671–684 (2024).
105. A. Jimenez, K. Friedl, C. Leterrier, About samples, giving examples: Optimized single molecule localization microscopy. *Methods* **174**, 100–114 (2020).
106. P. Webster, A. Webster, "Cryosectioning fixed and cryoprotected biological material for immunocytochemistry" in *Electron Microscopy: Methods and Protocols*, J. Kuo, Ed. (Humana Press, 2014), pp. 273–313.
107. E. Nehme, L. E. Weiss, T. Michaeli, Y. Shechtman, Deep-STORM: Super-resolution single-molecule microscopy by deep learning. *Optica* **5**, 458–464 (2018).
108. W. Ouyang, A. Aristov, M. Lelek, X. Hao, C. Zimmer, Deep learning massively accelerates super-resolution localization microscopy. *Nat. Biotechnol.* **36**, 460–468 (2018).
109. M. A. Ricci, C. Manzo, M. F. García-Parajo, M. Lakadamyali, M. P. Cosma, Chromatin fibers are formed by heterogeneous groups of nucleosomes in vivo. *Cell* **160**, 1145–1158 (2015).
110. M. Marenda, E. Lazarova, S. Linde, N. Gilbert, D. Michieletto, Parameter-free molecular super-structures quantification in single-molecule localization microscopy. *J. Cell Biol.* **220**, e202010003 (2021).
111. P. A. Gómez-García *et al.*, Mesoscale modeling and single-nucleosome tracking reveal remodeling of clutch folding and dynamics in stem cell differentiation. *Cell Rep.* **34**, 108614 (2021).
112. A. S. Hansen, I. Pustova, C. Cattoglio, R. Tjian, X. Darzacq, CTCF and cohesin regulate chromatin loop stability with distinct dynamics. *Elife* **6**, e25776 (2017).
113. B. Gu *et al.*, Opposing effects of cohesin and transcription on CTCF organization revealed by super-resolution imaging. *Mol. Cell* **80**, 699–711.e7 (2020).
114. M. Gelléri *et al.*, True-to-scale DNA-density maps correlate with major accessibility differences between active and inactive chromatin. *Cell Rep.* **42**, 112567 (2023).
115. B. Arnold *et al.*, Rapid depletion and super-resolution microscopy reveal an unexpected role of the nuclear-speckle protein SRSF5 in paraspeckle assembly and dynamics during cellular stress. bioRxiv [Preprint] (2024). https://doi.org/10.1101/2024.08.11.607506 (Accessed 29 May 2025).
116. J. Schindelin *et al.*, Fiji: An open-source platform for biological-image analysis. *Nat. Methods* **9**, 676–682 (2012).
117. F. Stehr *et al.*, Tracking single particles for hours via continuous DNA-mediated fluorophore exchange. *Nat. Commun.* **12**, 1–8 (2021).
118. J. Stein, tkPAINT datasets. Zenodo. https://doi.org/10.5281/zenodo.16411486. Deposited 24 July 2025.